Tellus (1997), 49A, 119–138
Printed in UK – all rights reserved

TELLUS
ISSN 0280–6495

An accurate interpolating scheme for semi-Lagrangian advection on an unstructured mesh for ocean modelling

By DANIEL Y. LE ROUX[1,2], CHARLES A. LIN[1,2]* and ANDREW STANIFORTH[3], [1]*Department of Atmospheric and Oceanic Sciences, and Center for Climate and Global Change Research, McGill University, Montréal, Québec, Canada, H3A 2K6;* [2]*Centre de Recherche en Calcul Appliqué (CERCA), 5160, boul. Décarie, bureau 400, Montréal, Québec, Canada, H3X 2H9;* [3]*Recherche en prévision numérique, Environnement Canada, 2121, route Trans-canadienne, Dorval, Québec, Canada, H9P 1J3*

(Manuscript received 27 July 1995; in final form 9 April 1996)

ABSTRACT

The semi-Lagrangian method is used for advection experiments on an irregular grid. A cosine hill is advected using a specified flow field corresponding to solid body rotation. A major difficulty is to find an interpolator which is at least fourth order accurate on an unstructured mesh. Such accuracy is needed for the treatment of Rossby waves in ocean models. We develop such a method using a dual kriging interpolating scheme. The results are better than fourth order accurate, as shown by comparison with bicubic spline interpolation on a structured grid. Such accuracy is maintained for an unstructured triangular grid. The dissipation and dispersion of the cosine hill remain small, even after many rotation periods. The increase in computational cost is significant even if the interpolation is performed separately on smaller subdomains. However, by taking advantage of the increased flexibility of unstructured meshes and accuracy of the kriging approach, it is possible to achieve the same accuracy at a reasonable computational cost compared to traditional methods.

1. Introduction

The understanding of the circulation of the world ocean requires the ability to model the interaction of many physical processes on an irregular domain. As the governing equations are nonlinear, accurate numerical techniques are needed for the solution of nonlinear partial differential equations. Current large scale models used for ocean and climate studies are usually based on finite differencing techniques for spatial discretization, and the classical leap frog scheme for time stepping. We propose to combine for the first time in ocean modelling the finite element and semi-Lagrangian methods on unstructured meshes. Advantages of the finite element method include the inherent flexibility of triangulation, which leads to almost homogeneous grids for domains with irregular boundaries. The semi-Lagrangian method of advection allows the use of a longer time step than that permitted by the Courant–Friedrichs–Lewy (CFL) stability criterion; it also gives very good phase speed with little numerical dispersion.

The explicit leap-frog scheme has a time step which is limited by the propagation speed of gravitational oscillations. A semi-implicit discretization of the terms responsible for these oscillations allows larger time steps (Robert et al., 1972). Further improvement is achieved through the use of the semi-Lagrangian method. Robert (1981, 1982) used a semi-Lagrangian treatment of advection combined with a semi-implicit treatment of gravitational oscillations in atmospheric models.

* Corresponding author.

He showed that a further factor of 6 is realized in the maximum stable time step compared to semi-implicit Eulerian schemes, without degrading the accuracy of the solution. Temperton and Staniforth (1987) gained another factor of 2 by using a 2 instead of a 3-time level scheme. It is very important to correctly determine the trajectories to at least second-order accuracy in time (Staniforth and Pudykiewicz, 1985; McDonald, 1987). Pudykiewicz and Staniforth (1984), Staniforth and Temperton (1986) and Temperton and Staniforth (1987) also showed that the semi-Lagrangian method can be profitably coupled to a finite element spatial discretization. A review of semi-Langrangian integration schemes for atmospheric models can be found in Staniforth and Côté (1991).

In this paper, we take a first step toward the combined use of the finite element and semi-Lagrangian methods in ocean modelling, by developing an accurate and flexible interpolating method. The latter is based on the dual kriging scheme. The paper is organised as follows. Section 2 is a brief description of the semi-Lagrangian method. The relative merits of interpolation with quadrilaterals and triangles are discussed in Section 3. Section 4 describes an interpolating scheme based on kriging. The results of advection experiments for rectangular and triangular meshes are respectively discussed in Sections 5 and 6, and the computational cost of kriging in Section 7. The conclusions are presented in Section 8.

2. The semi-Lagrangian advection scheme

Semi-Lagrangian advection is closely related to the particle-in-cell (Raviart, 1985; Bermejo, 1990) and characteristic Galerkin advection methods (Morton, 1985). While most Eulerian methods treat time and space as though they are unrelated, with exceptions such as the Lax–Wendroff scheme, characteristic methods interpret the time derivative at mesh nodal locations as the rate of change along flow characteristics. Similarly, semi-Lagrangian advection is treated using time differences along particle trajectories. The essence of this hybrid treatment is to get the best of the regular resolution of Eulerian schemes and the enhanced stability of Lagrangian methods. A different set of particles is selected at each time step, and we require that at the end of the time step, they arrive precisely at the mesh nodes. By tracking the particle back over that time step, we can locate its position at the previous time step using an approximate trajectory. An interpolation formula is then used to determine the upstream value of an advected scalar field.

In Fig. 1, the straight line (A'C) approximates the exact trajectory (AC) which arrives at mesh point x_m at time $t_n + \Delta t$. The particle is displaced by an amount α_m in the x-direction during the time interval Δt. If ϕ represents a scalar field, its Lagrangian derivative in 2-dimensions can be written as:

$$\frac{D\phi}{Dt} \equiv \frac{\partial \phi}{\partial t} + \boldsymbol{V}(\boldsymbol{X},t)\cdot\nabla\phi = \frac{\phi(\boldsymbol{X}_m, t_n+\Delta t) - \phi(\boldsymbol{X}_m - \alpha_m, t_n)}{\Delta t}, \quad (1)$$

where $\boldsymbol{X} = (x, y)$ is the position vector, and the advecting velocity field $\boldsymbol{V} = (u, v)$ is:

$$\frac{D\boldsymbol{X}}{Dt} = \boldsymbol{V}(\boldsymbol{X}, t). \quad (2)$$

The displacements $\boldsymbol{\alpha}_m$ are determined by an approximate integration of (2), following Staniforth and Côté (1991):

$$\boldsymbol{\alpha}_m = \Delta t \boldsymbol{V}^*\left(\boldsymbol{X}_m - \frac{\boldsymbol{\alpha}_m}{2}, t + \frac{\Delta t}{2}\right). \quad (3)$$

In order to have sufficiently accurate $O(\Delta t^2)$ estimates of the trajectory, Temperton and Staniforth (1987), and McDonald and Bates (1987) proposed the following 2-step process:

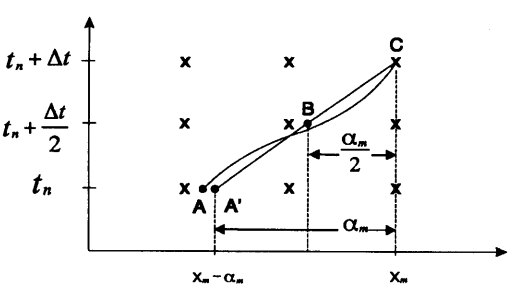

Fig. 1. A two-time-level semi-Lagrangian advection scheme. Approximate (A'C) and exact (AC) trajectories arrive at node x_m at time $t_n + \Delta t$. Here, α_m is the displacement of the particle in the x-direction in time Δt.

1. Extrapolate the velocity field at all nodes at time $(t+\frac{1}{2}\Delta t)$ by using a 2-time level scheme:

$$\boldsymbol{V}^*\left(\boldsymbol{X}, t+\frac{\Delta t}{2}\right)=\frac{3}{2}\boldsymbol{V}(\boldsymbol{X}, t) - \frac{1}{2}\boldsymbol{V}(\boldsymbol{X}, t-\Delta t)+\mathrm{O}(\Delta t^2). \quad (4)$$

2. Solve (3) iteratively, using interpolation when evaluating the right-hand side.

Only small differences were found between linear and cubic interpolation in the trajectory computations of step 2 above. A sufficient condition for convergence of (3) is given in Pudykiewicz et al. (1985):

$$\Delta t_{\max}(|u_x|, |v_y|, |u_y|, |v_x|) < 1. \quad (5)$$

Once the position of the departure point is known, the value of the scalar field ϕ at this location is found by interpolation. We discuss in the next section interpolation schemes using quadrilaterals and triangles.

3. Interpolation with quadrilaterals and triangles

The accuracy of the advection term depends on the choice of interpolation scheme for the semi-Lagrangian method. A difficulty is to find a 4th-order accurate interpolator. Such accuracy is needed in ocean modelling for the treatment of Rossby waves, which are intrinsically associated with advection; this is especially true in regions of boundary currents. Interpolation using different polynomials has been used in regular domains; these include linear, quadratic, cubic and quintic Lagrange polynomials, and bicubic spline formulations. The bicubic spline interpolation, which gives 4th-order spatial truncation errors with little damping, has been found to be a good compromise between accuracy and computational cost (Purnell, 1976; Bates and McDonald, 1982; McDonald, 1984; Pudykiewicz and Staniforth, 1984). Leslie and Purser (1991) obtained further accuracy using quintic interpolation, and Purser and Leslie (1988) recommended at least cubic interpolation.

Experiments with semi-Lagrangian advection carried out in an atmospheric context have typically used Cartesian meshes, thus preserving orthogonality between mesh elements. In this case, bicubic spline interpolation with orthogonal rectangular elements yields a 4th-order accurate $\mathrm{O}(\Delta x^4)$ result. This can be shown by considering the 16 nodes of the 9 rectangles surrounding the interpolation point. In ocean modelling, the situation can be quite different due to the presence of irregular coastlines. This means that the orthogonality between elements consisting of arbitrary quadrilaterals is not preserved, and an $\mathrm{O}(\Delta x^4)$ accuracy is no longer guaranteed.

To estimate the loss of accuracy due to non-orthogonal elements, we have performed advection experiments (Pudykiewicz and Staniforth, 1984) using different quadrilateral meshes with 33×33 nodes. They are obtained by smoothly deforming the uniform orthogonal mesh 1 shown in Fig. 2a. We present the results obtained for one of them, mesh 2, shown in Fig. 2b. All non-orthogonal elements have a distortion of $\pm\Delta x/8$ in the x-direction for each element, with the element area being preserved. The reference mesh 1 is a uniform mesh with an arbitrarily chosen grid spacing of $\Delta x = 10^5$ m. We solve for the time evolution of a scalar field ϕ subject to pure advection:

$$\frac{\mathrm{D}\phi}{\mathrm{D}t} \equiv \frac{\phi(\boldsymbol{X}_m, t_n+\Delta t)-\phi(\boldsymbol{X}_m-\boldsymbol{\alpha}_m, t_n)}{\Delta t}=0. \quad (6)$$

Initially, ϕ is a cosine hill centered at the point $(x_0, y_0) = (9, 17)$ of the 33×33 mesh, with a diameter of $8\Delta x$ in the x- and y-directions:

$$\phi(x, y)=\begin{cases} 50\left(1+\cos\dfrac{\pi R}{4\Delta x}\right) & \text{if } R \leqslant 4\Delta x \\ 0 & \text{otherwise,} \end{cases} \quad (7)$$

where $R^2=(x-x_0)^2+(y-y_0)^2$. The advecting velocity field is constant in time, and corresponds to solid body rotation with a prescribed angular frequency $\Omega = 10^{-5}\,\mathrm{s}^{-1}$ about the central point (17, 17) of the mesh:

$$u=-\Omega y \quad \text{and} \quad v=+\Omega x. \quad (8)$$

The Courant number $(C \equiv \max|\boldsymbol{V}|\Delta t/\Delta x)$ is set to unity. Here, $\max|\boldsymbol{V}|$ is the maximum speed among all nodes, which occurs at the four corners of the domain. One rotation of the cosine hill corresponds to 142 time steps. The values of Δx and Ω are chosen so that a comparison can be made with the results obtained by Pudykiewicz

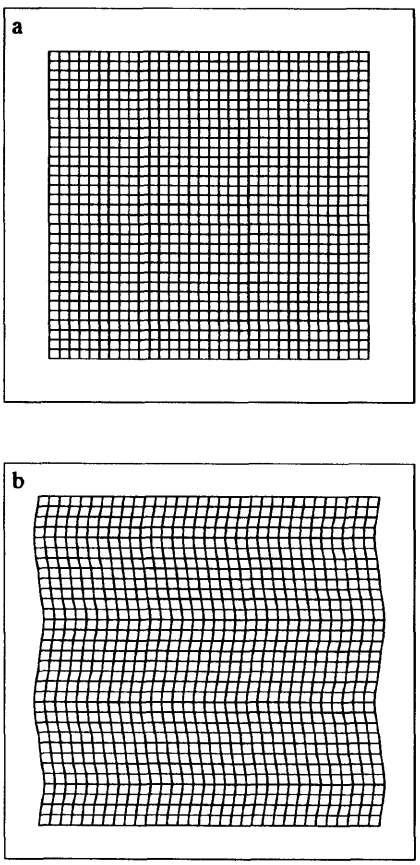

Fig. 2. (a) Mesh 1, with orthogonality between elements. (b) Mesh 2 is obtained from mesh 1 through a smooth deformation, which degrades orthogonality between elements.

and Staniforth (1984) in an atmospheric context. A simple scaling can provide more realistic ocean parameters without changing the results.

For meshes 1 and 2 the value $\phi(\boldsymbol{X}_m - \boldsymbol{\alpha}_m, t_n)$ of ϕ at the foot of each characteristic is obtained by first determining the displacements using the 2-time-level iterative scheme described earlier. Due to the loss of orthogonality for mesh 2, exact displacements are calculated from (2) and (8):

$$\boldsymbol{\alpha}_m = \begin{pmatrix} 1-\cos\Omega\Delta t & -\sin\Omega\Delta t \\ \sin\Omega\Delta t & 1-\cos\Omega\Delta t \end{pmatrix} \boldsymbol{X}_m, \tag{9}$$

where $\boldsymbol{X}_m$ is the position vector at the arrival point. A bicubic spline interpolation is then used to determine the value $\phi(\boldsymbol{X}_m - \boldsymbol{\alpha}_m, t_n)$ at each departure point. This procedure is repeated at each time step. Note that (9) is used only in Section 3 to compute displacements for the non-orthogonal grid. For the rectangular and triangular meshes of Sections 5 and 6, eq. (3) is solved iteratively with linear interpolation.

Table 1 shows the maximum ($\phi_{\max}$) and minimum ($\phi_{\min}$) values of ϕ, the change in mass, and the root mean square error (RMS) of the cosine hill after one rotation on meshes 1 and 2. The latter quantity is defined as:

$$\mathrm{RMS}(\phi) = \frac{\int_\Omega (\phi(t) - \phi(0))^2 \, \mathrm{d}\Omega}{\int_\Omega \phi^2(0) \, \mathrm{d}\Omega}. \tag{10}$$

We see that there is a significant impact of the loss of orthogonality: the dissipation and undershoot become larger for mesh 2, and there is now a significant loss of mass. The loss of accuracy is entirely due to the evaluation of upstream tracer values (using bicubic spline interpolation), since the displacements are solved exactly through (9). This loss of accuracy arises because the coefficients of the bicubic spline interpolation are derived for an orthogonal grid; it is not clear how these coefficients can be better determined for a non-orthogonal grid.

Aside from the loss of accuracy due to the non-orthogonal nature of the mesh, the use of arbitrary quadrilaterals for ocean modelling has other difficulties. As the ocean topology consists of irregular coastlines and islands, it is difficult to generate a homogeneous mesh with quadrilaterals.

Table 1. *Maximum, minimum, ratio of mass variation and the root mean square error of the cosine hill after 1 rotation using bicubic spline interpolation on meshes 1 and 2, $R = 4\Delta x$, $C = 1$*

Mesh	1	2
$\phi_{\max}$	90.5	81.3
$\phi_{\min}$	−3	−3.2
$\dfrac{\int \phi(t)}{\int \phi(0)}$	1.000	0.761
RMS(ϕ)	0.015	0.128

Such a mesh would likely be less flexible than a triangular mesh. The importance of a homogeneous mesh is fundamental, especially for problems involving wave propagation, in order to avoid spurious refraction and reflection due to the mesh. The solution of interest in ocean modelling often involves intense boundary currents. In such cases, spurious reflection due to the mesh can become an important issue. For these reasons, we have adopted triangular elements in the present work, thus retaining the flexibility and homogeneity of the mesh. However, we need to find an interpolation scheme with $O(\Delta x^4)$ accuracy for an unstructured triangular mesh.

Triangular meshes have been examined in the past for atmospheric modelling. Sadourny et al. (1968) and Williamson (1968) used spherical triangulation in studies of the nondivergent barotropic vorticity equation. This approach was later extended to the barotropic primitive equations by Williamson (1970), Sadourny (1972) and Cullen (1974). Triangular grids are obtained by making subdivisions in a latitude-longitude plane of the 20 and 12 faces of an imbedded regular icosahedron or dodecahedron. This procedure has been further improved by Baumgardner and Frederickson (1985) by constructing a grid on the surface of the two-sphere, instead of projecting the 2-sphere onto a latitude–longitude plane. They were then able to generalize the piecewise linear finite elements to spherical triangles by defining a local system of barycentric coordinates. More recently, Baumgardner (1994, private communication) applied this spherical triangulation together with an implicit semi-Lagrangian method to the shallow water equations. A 2nd-order monotone interpolation procedure is used for advection, using field values at the vertices and midpoints of the sides of each triangle. In another recent study, Heikes and Randall (1995a, b) solved the shallow-water equations on a twisted icosahedral grid where a Voronoi cell is associated with each vertex of the polyhedra. It would likely be difficult to use this triangular mesh for an oceanic geometry, due to the presence of irregular coastlines and islands. Furthermore, it is restricted to uniform meshes, and local refinements are not possible without breaking the continuity between elements. In another study, Karpic (1994) used the Lagrangian–Galerkian method with a triangular mesh. A spline-based approach is being examined to avoid stability problems due to inexact quadrature evaluation.

4. A kriging interpolating scheme

We have seen in Section 3 that the interpolation accuracy using bicubic spline is sensitive to the deformation of a rectangular grid. Since we seek to interpolate on an unstructured mesh, a more appropriate interpolating scheme would be one which does not depend on the geometry, but only on the nodal positions. The use of distance weighting functions, where larger weights are assigned to closer grid points, is a first step in this direction. However, the choice of the distance weighting function is somewhat arbitrary. Other more sophisticated algorithms are available, such as analysis methods, which are well adapted to unstructured meshes. An example of the latter is the use of polynomial interpolators, which gives a surface fitting the data points exactly. Any such analysis method that fits the data points may be used as an interpolator for the semi-Lagrangian advection method. The choice is dictated by a compromise between the flexibility and complexity of the method, its accuracy and computational cost. The kriging scheme is one such possibility. In the past, the kriging technique has been widely used in seismology and is closely related to optimal or statistical interpolation (Lorenc, 1986; Daley, 1991). In fact, most of the methods which have been proposed for analysis for numerical weather prediction such as optimal interpolation, kriging, splines, successive corrections, Kalman–Bucy filters, can be related to one other. As the use of kriging is not common in oceanic modelling, we describe its main features here.

The term "kriging" was attributed to Matheron (1973) to honor the pioneering work of Krige (1951) in the early 1950s. It can be summarised as being the best linear unbiased estimator of a random function. Kriging assumes that a physical phenomenon may be represented by a random function $F(\boldsymbol{X})$ in the vector space $\boldsymbol{U}$ of random variables, where $\boldsymbol{X} = x$, $\boldsymbol{X} = (x, y)$, or $\boldsymbol{X} = (x, y, z)$ is the respective position vector in 1-, 2- and 3-dimensions. Consider a series of N measurements f_i of the phenomenon at different locations $\boldsymbol{X}_i$, $1 \leqslant i \leqslant N$. Kriging constructs an approximate function of $F(\boldsymbol{X})$, known as the surface model

$f(\boldsymbol{X})$, such that:

$$f(\boldsymbol{X}_i) = f_i, \qquad 1 \leqslant i \leqslant N. \tag{11}$$

The simplest choice of $f(\boldsymbol{X})$ is a linear combination of the data with weights θ_i to be determined later:

$$f(\boldsymbol{X}) = \sum_{i=1}^{N} \theta_i f_i. \tag{12}$$

The precise determination of $f(\boldsymbol{X})$ will be given later in the discussion of the dual kriging method. The kriging approach is to split the unknown random function $F(\boldsymbol{X})$ into the sum of a mean value or drift $a(\boldsymbol{X})$, and a fluctuation or error term $b(\boldsymbol{X})$:

$$F(\boldsymbol{X}) = a(\boldsymbol{X}) + b(\boldsymbol{X}). \tag{13}$$

The drift is generally represented by a polynomial in x, y and z, or by trigonometric functions (Gilbert et al., 1990). More generally, the drift belongs to a subspace $\boldsymbol{P} \subset \boldsymbol{U}$, spanned by M basis functions $p_k(\boldsymbol{X})$:

$$a(\boldsymbol{X}) = \sum_{k=1}^{M} a_k p_k(\boldsymbol{X}). \tag{14}$$

The efficiency of kriging comes in part from the fact that the drift follows the physical phenomenon. The correction term $b(\boldsymbol{X})$ is then adjusted so that the interpolation function fits the data points exactly; kriging *is thus a true interpolator.* The appropriate equations can be derived in several steps (Delfiner and Delhomme, 1973; Trochu, 1993).

(1) The no-bias conditions states that the mean value of the random function ($E[F(\boldsymbol{X})]$) is the same as that of the linear combination of the random variables, with weights θ_i:

$$E[F(\boldsymbol{X})] = E\left[\sum_{i=1}^{N} \theta_i F(\boldsymbol{X}_i)\right]. \tag{15}$$

Since E is a linear operator and $b(\boldsymbol{X})$ represents a fluctuation having a zero mean, the conditions of no-bias become:

$$a(\boldsymbol{X}) = \sum_{i=1}^{N} \theta_i a(\boldsymbol{X}_i), \tag{16}$$

for all drift functions $a(\boldsymbol{X}) \in \boldsymbol{P}$. In particular, (16) must be true for the basis functions $p_k(\boldsymbol{X})$ which gives:

$$\sum_{i=1}^{N} \theta_i p_k(\boldsymbol{X}_i) = p_k(\boldsymbol{X}) \qquad \text{for} \qquad 1 \leqslant k \leqslant M. \tag{17}$$

(2) The weights θ_i are chosen to minimize the squared variance of the estimation error:

$$E\left[F(\boldsymbol{X}) - \sum_{i=1}^{N} \theta_i F(\boldsymbol{X}_i)\right]^2$$
$$= E[F(\boldsymbol{X})]^2 - 2\sum_{i=1}^{N} \theta_i E[F(\boldsymbol{X})F(\boldsymbol{X}_i)]$$
$$+ \sum_{i,j=1}^{N} \theta_i \theta_j E[F(\boldsymbol{X}_i)F(\boldsymbol{X}_j)] \tag{18}$$

subject to the conditions of no-bias (17) as constraints. This minimization is thus equivalent to minimizing a quadratic expression with respect to θ_i, subject to the M linear constraints of (17). This leads to the solution of a linear system with $M + N$ unknowns $(\theta_1, \ldots, \theta_N; \mu_1, \ldots, \mu_M)$, where the additional unknowns μ_k are the Lagrange multipliers associated with the constraints. The minimization, carried out in the standard way through partial differentiation with respect to θ_i, results in the first part of the following system of equations. The second part is the no-bias conditions.

$$\begin{cases} E[F(\boldsymbol{X})F(\boldsymbol{X}_i)] = \displaystyle\sum_{j=1}^{N} \theta_j E[F(\boldsymbol{X}_i)F(\boldsymbol{X}_j)] + \sum_{k=1}^{M} \mu_k p_k(\boldsymbol{X}_i) \\ \qquad\qquad \text{for} \quad 1 \leqslant i \leqslant N \\ \displaystyle\sum_{j=1}^{N} \theta_j p_k(\boldsymbol{X}_j) = p_k(\boldsymbol{X}) \\ \qquad\qquad \text{for} \quad 1 \leqslant k \leqslant M. \end{cases} \tag{19}$$

(3) To solve the system (19), we must specify the form of the covariance $E[F(\boldsymbol{X}_i)F(\boldsymbol{X}_j)]$. It is assumed to depend on only the Euclidean distance h between $\boldsymbol{X}_i$ and $\boldsymbol{X}_j$:

$$h_i(\boldsymbol{X}_j) = |\boldsymbol{X}_i - \boldsymbol{X}_j| = \sqrt{(x_i - x_j)^2 + (y_i - y_j)^2}. \tag{20}$$

The covariance can thus be represented by a function $K(h)$, known as the generalized covariance. However, not all functions can serve as a generalized covariance. As the mean square variance of the estimation error is non-negative, the quadratic form (18) must remain positive. This places some restriction on the possible choices of the generalized covariance. Furthermore, it can be shown that if the quadratic form (18) is positive definite, the solution $(\theta_1, \ldots, \theta_N; \mu_1, \ldots, \mu_M)$ of the kriging system (19) exists and is unique.

The kriging system (19) can be written in matrix

form as:

$$\left(\begin{array}{c|c} K_{ij} & p_k(X_i) \\ \hline p_k(X_j) & 0 \end{array}\right)\left(\begin{array}{c} \theta_1 \\ \vdots \\ \theta_N \\ \hline \mu_1 \\ \vdots \\ \mu_M \end{array}\right)=\left(\begin{array}{c} K_1 \\ \vdots \\ K_N \\ \hline p_1(X) \\ \vdots \\ p_M(X) \end{array}\right), \tag{21}$$

where $K_i = K(h_i(X))$ and $K_{ij} = K(h_i(X_j))$. Eq. (21) is known as the primal kriging system. Note that the kriging matrix in (21) is symmetric. The value $f(X)$ at each node is then obtained by substitution of θ_i, $1 \leqslant i \leqslant N$, in (12).

Kriging is a local interpolation method since interpolation at each node requires the solution of a new kriging linear system, as the local coordinate X is found explicitly on the right hand side of (21). However, when large data sets are used, as is usually the case in oceanography, an alternative known as dual kriging may be more appropriate, as the system is solved only once to obtain the surface model $f(X)$ explicitly. This is done by formulating a dual kriging system which is strictly equivalent to the primal system, and where the right hand side of the dual system does not depend on the local coordinate. We now describe how the dual system is obtained and demonstrate its equivalence with the primal system. We do this by suitable algebraic manipulations (Trochu, 1993).

The inversion of (21) leads to the following solution with the appropriate matrices A, B, C indicated schematically:

$$\left(\begin{array}{c} \theta_1 \\ \vdots \\ \theta_N \\ \hline \mu_1 \\ \vdots \\ \mu_M \end{array}\right)=\left(\begin{array}{c|c} A & B \\ \hline B^{\mathrm{T}} & C \end{array}\right)\left(\begin{array}{c} K_1 \\ \vdots \\ K_N \\ \hline p_1(X) \\ \vdots \\ p_M(X) \end{array}\right). \tag{22}$$

After substitution for the coefficients θ_i, $1 \leqslant i \leqslant N$, in (12), we obtain the surface model $f(X)$ in matrix form:

$$f(X) = (f_1 \ldots f_N)A\begin{pmatrix} K_1 \\ \vdots \\ K_N \end{pmatrix} + (f_1 \ldots f_N)B\begin{pmatrix} p_1(X) \\ \vdots \\ p_M(X) \end{pmatrix}. \tag{23}$$

Note that the inverse kriging matrix in (22) is symmetric as the coefficient matrix in (21) is itself symmetric. Thus the $N \times N$ matrix A is also symmetric. We define the variables λ_i and a_i, $1 \leqslant i \leqslant N$, which now replace θ_i and μ_i as unknowns to be determined:

$$\begin{pmatrix} \lambda_1 \\ \vdots \\ \lambda_N \end{pmatrix} = A\begin{pmatrix} f_1 \\ \vdots \\ f_M \end{pmatrix}, \qquad \begin{pmatrix} a_1 \\ \vdots \\ a_M \end{pmatrix} = B^{\mathrm{T}}\begin{pmatrix} f_1 \\ \vdots \\ f_M \end{pmatrix}. \tag{24}$$

Eq. (23) then becomes:

$$f(X) = \sum_{k=1}^{M} a_k p_k(X) + \sum_{j=1}^{N} \lambda_j K(h_j(X)). \tag{25}$$

The above is an explicit representation of the dual kriging model, which gives $f(X)$ at any location X.

We can combine and rewrite (24) in matrix form as:

$$\left(\begin{array}{c} \lambda_1 \\ \vdots \\ \lambda_N \\ \hline a_1 \\ \vdots \\ a_M \end{array}\right)=\left(\begin{array}{c|c} A & Q \equiv B \\ \hline B^{\mathrm{T}} & R \equiv C \end{array}\right)\left(\begin{array}{c} f_1 \\ \vdots \\ f_N \\ \hline 0 \\ \vdots \\ 0 \end{array}\right), \tag{26}$$

where the matrices Q and R are arbitrary, as they are multiplied by the null vector on the right hand side. By a suitable choice of these matrices, we can demonstrate the equivalence of the primal and dual kriging systems. In fact, by setting $Q \equiv B$ and $R \equiv C$ as indicated in (26), the coefficient matrix in (22) and (26) become identical. However, the coefficient matrix in (22) is precisely the inverse of the coefficient matrix in the primal kriging system (21). The coefficients a_k, $1 \leqslant k \leqslant M$, and

λ_j, $1 \leqslant j \leqslant N$ are thus solutions of:

$$\left(\begin{array}{c|c} K_{ij} & p_k(\boldsymbol{X}_i) \\ \hline p_k(\boldsymbol{X}_j) & 0 \end{array}\right)\left(\begin{array}{c} \lambda_1 \\ \vdots \\ \lambda_N \\ \hline a_1 \\ \vdots \\ a_M \end{array}\right)=\left(\begin{array}{c} f_1 \\ \vdots \\ f_N \\ \hline 0 \\ \vdots \\ 0 \end{array}\right). \tag{27}$$

The linear system (27), which no longer has the right hand side dependent on $\boldsymbol{X}$, is the matrix form of the surface model (25). Together, they form the dual kriging formulation. We have thus shown the strict equivalence of the primal and dual kriging systems. Since the coefficient matrix and the right hand side in (27) depend only on the geometry and not on the local coordinate, a LU decomposition needs only to be performed once, even for non-steady problems. It is now possible to interpolate for any point in the convex envelope of the domain. We again emphasize that kriging is a true interpolator, as the interpolation matches the values at the data points.

In forming the generalized covariance, polynomial models of odd degree (h^{2i+1}) have proven useful. A family of possible generalized covariance models using such polynomials is (Christakos, 1984):

$$K(h)=\sum_{i=0}^{m}(-1)^{i+1}b_i h^{2i+1}, \tag{28}$$

with positive coefficients b_i. In practice, for large values of m in (28), the kriging matrix in (27) may become ill-conditioned. For the experiments of Sections 5 and 6, the library LAPACK was used to estimate the condition number of the dual kriging matrix. The results varied too much with the domain scale and hence are not meaningful. However, the accuracy of the LU decomposition remains very good. An estimate of the accuracy was obtained by solving for the image of each column using the inverse kriging matrix. For typical domains of 1000 nodes of Sections 5 and 6, the accuracy ranged from one part in 10^{-7} to 10^{-13} for different choices of $K(h)$ ranging from h^7 to h.

Polynomials of even degree are not admissible, as the covariance is defined up to an even polynomial (Matheron, 1973). Furthermore, even degree polynomials are filtered by the no-bias conditions (Delfiner, 1979). The restrictions $b_i \geqslant 0$ are sufficient but not necessary conditions for the kriging matrix to be positive definite (Matheron, 1973).

The surface $f(x, y)$ and its derivatives can in principle be obtained analytically. However, the existence of non-singular derivatives up to order m depends on the choice of the function $K(h)$. For example, $K(h)=-h$ gives a continuous $f(x, y)$ which is not differentiable, as h depends on the square root of a distance. The choice $K(h)=h^3$ would give a once differentiable $f(x, y)$. This important property is usually not found with other interpolating schemes. For example, Lagrange interpolation polynomials are continuous but the interpolating functions are usually not differentiable.

We refer to Trochu (1993; his Fig. 3) for examples in 1-dimension of different covariance models for a given drift. For $K(h)=-h$, kriging reduces to the piecewise linear Lagrange finite elements, while it is equivalent to cubic spline interpolation with the choice $K(h)=h^3$. The Gaussian covariance $K(h)=\exp(-ch^2)$, with c being constant, is yet another possible choice. A more complete discussion of kriging can be found in Journel and Huijbregts (1978).

The drift and generalized covariance $K(h)$ can in general be chosen independently. However, Matheron and Duchon showed there is a relation between them, in the case when kriging reduces to spline interpolation. In 1-dimension, Matheron (1980) showed that a kriging interpolation with $K(h)=(-1)^{m+1}h^{2m+1}$ is identical to a spline interpolation which minimizes the simple operator $T=\mathrm{d}^{m+1}/\mathrm{d}x^{m+1}$ with $\boldsymbol{P}=\ker(T)$, i.e. the vector space $\boldsymbol{P}$ is the kernel of the operator T. The generalization to higher dimensions is not as simple because it is difficult to determine $\ker(T)$. However, Matheron (1980) did obtain the following result for the n-dimensional case. The spline function $f(x_1, \ldots, x_n)$ which minimizes:

$$\int_{\mathbb{R}^n}[\Delta^r f(x_1, \ldots, x_n)]^2\,\mathrm{d}x_1 \ldots \mathrm{d}x_n, \tag{29}$$

is identical to the solution of a kriging interpola-

tion with:

$$\boldsymbol{P} = \ker(\Delta^r) \qquad \text{and} \qquad \Delta^{2r} K(h) = \delta_{x_1,\ldots,x_n}. \tag{30}$$

Here, Δ is the Laplacian operator, and $\delta_{x_1,\ldots,x_n}$ is the Dirac measure at a point $(x_1, \ldots, x_n)$. The constraints $f(x_{1i}, \ldots, x_{ni}) = f_i$, $1 \leqslant i \leqslant N$, are provided by N known measurements. Kriging is thus a flexible interpolation method which reduces to spline interpolation as a special case. Dubrule (1981) and Trochu (1993) showed that the method of least squares is a limiting case as well, when the so-called *nugget* effect is introduced in kriging. This effect permits the incorporation of measurement errors in the analysis procedure. Matheron (1980) also showed that the following choice:

$$K(h) = \begin{cases} h^{4r-n} & \text{for } n \text{ odd} \\ h^{4r-n} \ln h & \text{for } n \text{ even,} \end{cases} \tag{31}$$

provides a new class of admissible generalized covariance models. For example, for $r = 1$ in (31), possible covariance models are $K(h) = h^3$, $K(h) = h^2 \ln h$ and $K(h) = h$ for $n = 1$, 2 and 3 dimensions respectively. We will use these covariance models in later sections.

5. Results and advection experiments: rectangular meshes

Most of the kriging applications we found in the literature deal with contouring, numerical cartography and 3-dimensional stress analysis. The generalized covariance used is usually a linear combination of h, $h^2 \ln h$ and h^3 for steady problems. Here, we apply dual kriging to advection experiments with the velocity field given by solid body rotation.

We start from the advection experiment described in Section 3. Different drifts and generalized covariances are used to obtain the surface $f(x, y)$ on mesh 1 with $R = 4\Delta x$; i.e, the initial cosine hill is resolved by a 7×7 stencil of points, where all points outside the stencil are identically zero. All the experiments described in this Section are done on mesh 1. We compare these results with those obtained with bicubic spline interpolation. Numerical dispersion eventually causes the cosine hill to reach the boundary, generating boundary problems due to the open boundary. The experiment then loses its validity and this is why we do not display results for bicubic spline interpolation after 5 rotations on the 33×33 mesh. In Section 7, we use meshes with more resolution and hence less numerical dispersion, thus extending the period of validity of the integration. With kriging, a similar restriction on the period of integration applies for certain choices of $K(h)$. With other choices of $K(h)$, there is much less dispersion and many more rotations of the cosine hill can be performed; and the corresponding results displayed.

Figs. 3 and 4 compare the maximum ($\phi_{\max}$) and minimum ($\phi_{\min}$) values of the cosine hill after up to 40 rotations. Recall that initially, $\phi_{\max} = 100$, $\phi_{\min} = 0$; these extreme values should be preserved by solid body rotation. Different choices of the function $K(h)$ and different drifts are used. Fig. 3 shows that for $\phi_{\max}$, kriging with $K(h) = -h$ and $K(h) = h^2 \ln h$, both with a linear drift, performs less well than a bicubic spline. However, other choices of $K(h)$ can lead to significantly better results in particular for $K(h) = h^3$ and $K(h) = -h^5$ with a linear and a quadratic drift respectively. For $K(h) = h^7$ and cubic drift, there is almost no attenuation of the maximum after 40 rotations. For $\phi_{\min}$, Fig. 4 shows that kriging gives better results, than bicubic spline interpolation for almost all choices of $K(h)$ and drifts.

From the above results, we see that $K(h) = h^7$ with cubic drift gives the best results. Fig. 5 shows the percentage of mass variation for this choice, after up to 40 rotations. Our results show that mass conservation is satisfied well with kriging.

To compare the order of the method using bicubic spline and kriging interpolation, Fig. 6 summarizes a mesh convergence study showing the decrease of the root mean square error as a function of the spatial resolution. The latter is measured by the element size $(A/N_{\text{el}})^{1/2}$, where A is the domain area, and N_{el} is the total number of elements. The results are displayed after one rotation of the cosine hill. They show that kriging with $K(h) = h^3$ is always more accurate than bicubic spline at all resolution. At intermediate resolution, where damping of the cosine hill is significant, kriging with $K(h) = h^5$ and $K(h) = h^7$ yields a higher order accuracy than bicubic spline. However the order becomes comparable at high resolution, when damping and dispersion become much smaller for both schemes. In the above experiments, the Courant number has been

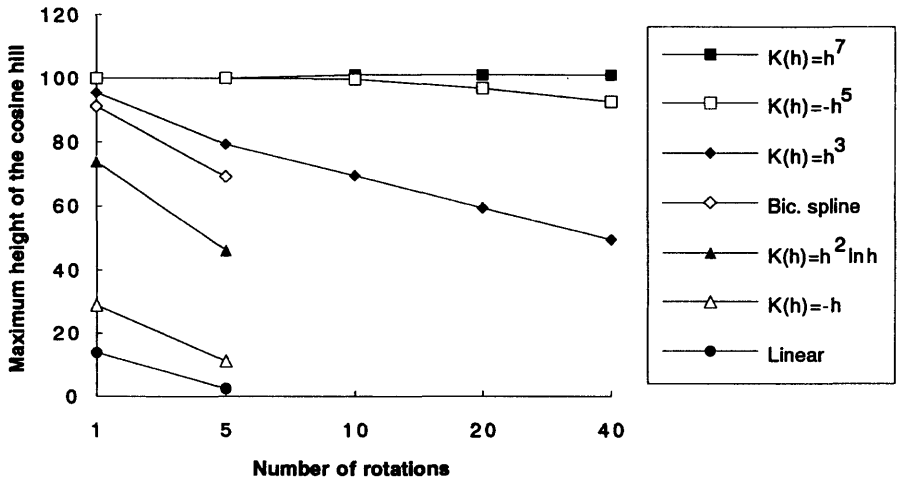

Fig. 3. Maximum values of the cosine hill after up to 40 rotations (5688 time steps) on mesh 1 using linear, bicubic spline and kriging interpolation (with different $K(h)$) schemes, $R = 4\Delta x$, $C = 1$.

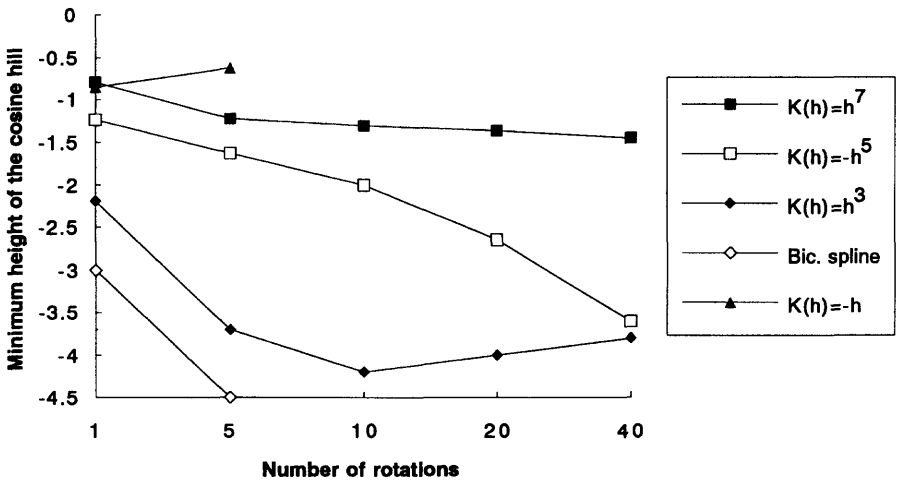

Fig. 4. Minimum values of the cosine hill after up to 40 rotations (5688 time steps) on mesh 1 using bicubic spline and kriging interpolation (with different $K(h)$) schemes, $R = 4\Delta x$, $C = 1$.

reduced from $C = 1$ to ensure the temporal truncation errors remain smaller than the spatial errors. We have also verified the above result obtained at high resolution is not due to increased inaccuracy of the LU decomposition of the kriging matrix.

An illustration of the actual cosine hill after 160 rotations or about 22 752 time steps with kriging is shown in Fig. 7d. Vertical cross-sections on the x, z plane are shown. The initial cosine hill is shown in Fig. 7a; Figs. 7b, c show the cosine hill after 5 rotations for bicubic spline interpolation and kriging, respectively. As with Fig. 5, results obtained with bicubic spline interpolation and kriging with $K(h) = h^7$ and cubic drift are compared. We see that the bicubic interpolation scheme leads to significant damping, whereas with kriging, the cosine hill retains almost its initial configuration even after 160 rotations (Fig. 7d).

For the results shown so far, it is the choice of the generalized covariance $K(h)$ that has the most

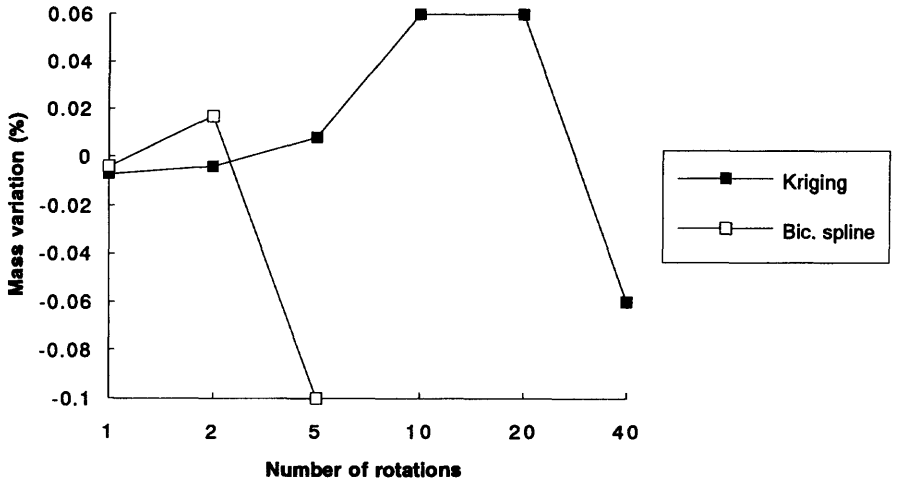

Fig. 5. Mass variation (%) of the cosine hill after up to 40 rotations (5688 time steps) on mesh 1 using bicubic spline and kriging interpolation ($K(h) = h^7$) schemes, $R = 4\Delta x$, $C = 1$.

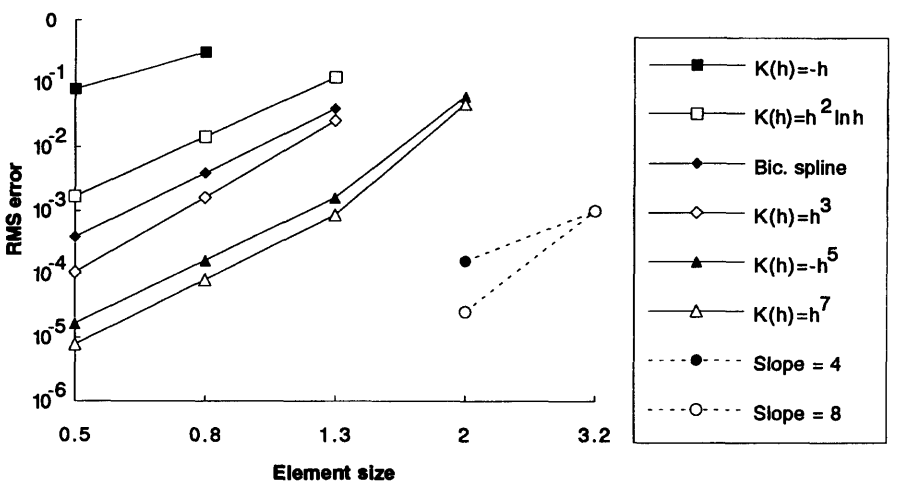

Fig. 6. RMS (ϕ) of the cosine hill after one rotation on mesh 1, as a function of the spatial resolution. The two dashed lines with slopes of 4 and 8 are shown for comparison.

impact on the accuracy, and not the drift. We have found that a linear drift reproduces almost exactly the results obtained using higher degree polynomials in the drift. We have also performed experiments with $K(h) = h^6 \ln h$ and $K(h) = -h^9$; the results are not significantly different from those obtained earlier with $K(h) = h^7$. Other experiments also indicate that the choice $K(h) = h^7$ is the preferred one. For example, when the number of nodes under the initial cosine hill is reduced from $R = 4\Delta x$, Table 2 shows that $K(h) = h^7$ performs better than $K(h) = -h^5$. For both choices, kriging tends to give better results than bicubic spline interpolation. There is little difference in computational cost between a high and low order $K(h)$. The cost of computing the drift is always negligible in comparison to the covariance. We discuss in Section 7 the computational cost of using kriging interpolation. For the remainder of this paper, we show the kriging results with the choice $K(h) = h^7$.

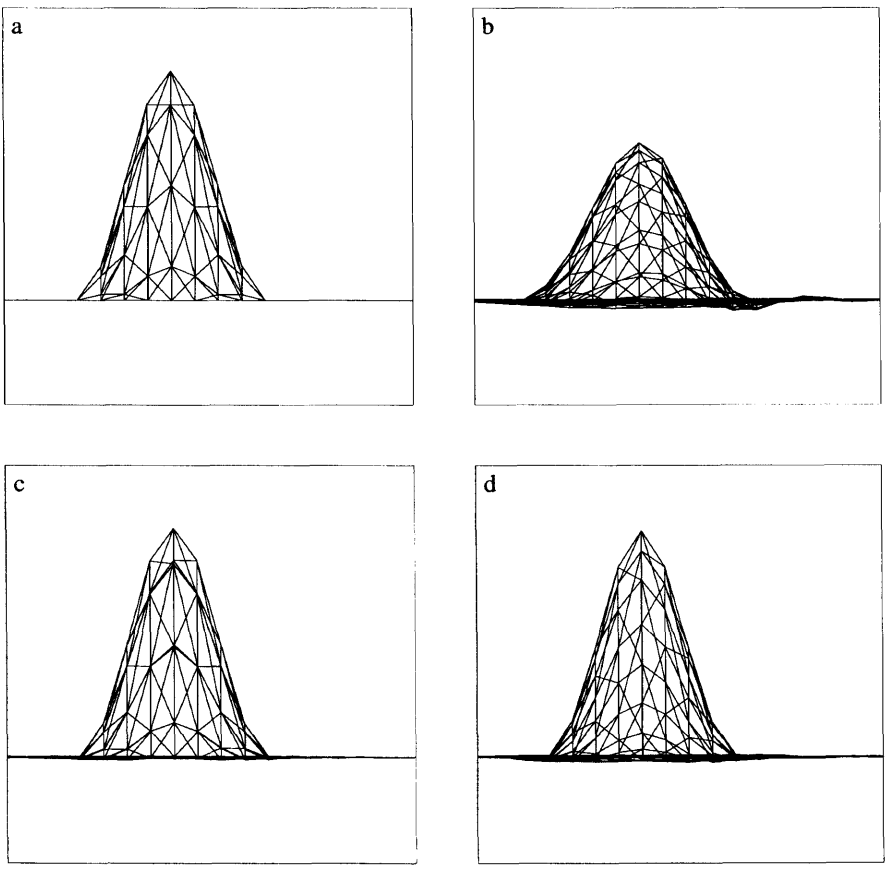

Fig. 7. (a) Shape of the cosine hill on mesh 1 at time $t = 0$, $R = 4\Delta x$; $(\phi_{max}, \phi_{min}) = (100, 0)$ indicated in brackets at later times. (b) After 5 rotations (711 time steps) using bicubic spline interpolation, $R = 4\Delta x$, $C = 1$; (69, −4.5). (c) After 5 rotations (711 time steps) using kriging interpolation scheme ($K(h) = h^7$, cubic drift) $R = 4\Delta x$, $C = 1$; (100, −1.2). (d) Same as Fig. 7c after 160 rotations (22 752 time steps); (99, −2.3).

Table 2. *Influence of the radius (R) of the cosine hill on its maximum and minimum values, after 5 rotations on mesh 1, for bicubic spline and kriging interpolation schemes, C = 1*

	R	ϕ_{max}	ϕ_{min}
bicubic spline	$2\Delta x$	25	−3.9
	$3\Delta x$	48	−5.6
$K(h) = -h^5$ quadratic drift	$2\Delta x$	59	−6.6
	$3\Delta x$	90	−4.5
$K(h) = h^7$ cubic drift	$2\Delta x$	75	−6.6
	$3\Delta x$	100	−2.1

We now consider an additional and more demanding advection experiment. The cosine hill with $R = 4\Delta x$ will be advected by a flow field with deformation which is centered at point (17, 17) of the 33 × 33 mesh 1, given by the streamfunction:

$$\psi = -\frac{LV_{max}}{4}\left(1 - \frac{4x^2}{L^2}\right)\cos\left(\frac{\pi y}{L}\right). \qquad (32)$$

The Courant number is $C = V_{max}\Delta t/\Delta x$ and we take $\Delta x = 10^5$ m, $L = 32\Delta x$ and $V_{max} = 30$ m s^{-1}.

Table 3 shows the maximum (ϕ_{max}) and minimum (ϕ_{min}) values, the normalized mass $\frac{\sum \phi(t)}{\sum \phi(0)}$ and variance $\frac{\sum \phi^2(t)}{\sum \phi^2(0)}$

Table 3. *Influence of the Courant number(C) in the case of an anisotropic rotation with strong deformation on mesh 1, for bicubic spline (upper rows) and kriging (lower rows, $K(h) = h^7$, cubic drift) interpolation schemes after 1 rotation, $R = 4\Delta x$*

	ϕ_{max}	ϕ_{min}	$\frac{\sum \phi(t)}{\sum \phi(0)}$	$\frac{\sum \phi^2(t)}{\sum \phi^2(0)}$	RMS(ϕ)
$C = 1$	85	−6.3	1.000	0.860	1.62×10^{-2}
	98	−3.5	1.000	0.992	8.23×10^{-4}
$C = 2$	87	−3.5	1.000	0.897	6.73×10^{-3}
	98	−2.5	1.000	0.992	8.24×10^{-4}
$C = 4$	93	−3.1	1.000	0.942	2.78×10^{-3}
	99	−2.6	1.000	0.995	5.72×10^{-4}

The last column shows the RMS error when the deformational flow is reverted after one half rotation, and the cosine hill is advected back to its initial position.

after 1 rotation, for three values of the Courant number $C = 1$, 2 and 4. This is a more stringent test than solid body rotation as the deformational flow will eventually deform the cosine hill to become subgrid scale. As before, we compare the results obtained with bicubic spline interpolation and kriging. Due to the strong deformation associated with the anisotropic flow field, the dispersion is now more severe than with solid body rotation. However, the kriging results still show less dispersion and damping.

The deformational flow is next reverted after one half rotation of the cosine hill, thus advecting the hill back to its initial position. Due to the hyperbolic nature of the advection equation, the cosine hill should be identical to its initial state at the end of the experiment, if the advection scheme were perfect. The RMS errors of this test are shown in the last column of Table 3, for bicubic spline interpolation and kriging. The results show a much better accuracy for kriging.

6. Results of advection experiments: triangular meshes

We now turn to the use of triangular elements. As mentioned already, the use of triangles for ocean models gives more flexibility than quadrilaterals in the treatment of irregular boundaries. We have thus triangulated an irregular domain, mesh 3, shown in Fig. 8a. This domain has the characteristics of an ocean basin: irregular coastlines, and the presence of an island and a peninsula. We repeat the same advection experiment of Section 5, using the dual kriging interpolation. The initial cosine hill at $t = 0$ is taken to be as in Fig. 7a. The result after 160 rotations, or 22 752 time steps, is shown in Fig. 8b. There is very little dispersion evident even after so many rotations. The results compare very well with those shown in Fig. 7d obtained with kriging on the rectangular mesh 1. The fact that kriging yields equally favourable results with triangles on an unstructured mesh and for quadrilaterals on a regular mesh demonstrates its excellent flexibility.

The 4th-order accuracy of the bicubic spline interpolation is lost close to the boundary of a regular mesh. To evaluate the loss of accuracy near a boundary when using the kriging interpolation we have triangulated a circle, mesh 4, shown in Fig. 9a. The same advection experiment of Section 5 is repeated with a half cosine hill centered on a point on the boundary of the domain. The half cosine hill defined at $t = 0$ is shown in Fig. 9b. After 10 000 time steps the maximum remains at 100 and the minimum becomes −2, as shown in Fig. 9c. Thus in this particular case, significant accuracy is retained near the boundary when using kriging.

7. The computational cost of kriging

The most costly part of the dual kriging calculation is in the evaluation of the surface model (25), and not in the LU decomposition of the kriging matrix to solve (27), for non-steady problems.

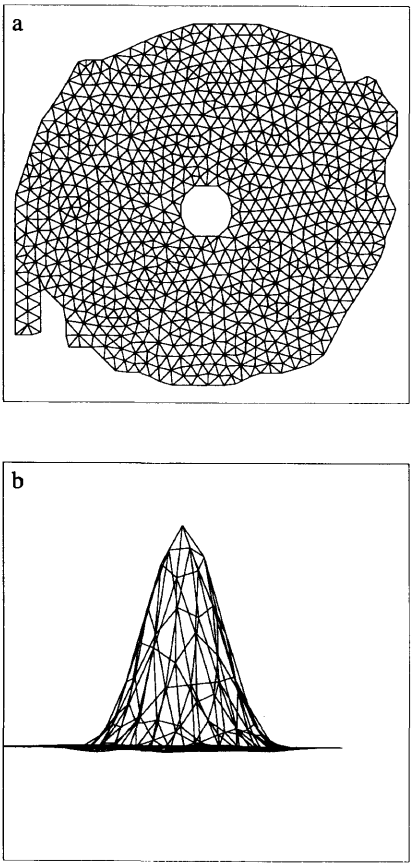

Fig. 8. (a) Mesh 3, an unstructured triangular grid with some characteristics of an ocean basin. (b) Shape of the cosine hill on mesh 3 after 160 rotations (22 752 time steps) using a kriging interpolation scheme ($K(h) = h^7$, cubic drift), $R = 4\Delta x$, $C = 1$, $\phi_{max} = 100$, $\phi_{min} = -2.3$.

This is because the kriging matrix of (27) only depends on the geometry, so that the LU decomposition is done only once and its cost becomes negligibly small once it is spread over a large number of time steps. Indeed, for a single field and a mesh of N nodes, there are $12N$ long operations (multiplications and divisions) and N square roots per time step per node in the calculation of (25), when $K(h) = h^7$. For $K(h) = -h^5$ and $K(h) = h^3$, there are $11N$ and $10N$ long operations respectively, and N square roots, per time step per node. The computational cost of the drift in (25) is not included in these estimates since it is independent of N and thus contributes marginally to the total cost. When the computation is optimised by using nested multiplication, there are 4, 10 and 20 operations (additions and multiplications) for linear, quadratic and cubic drifts, respectively.

The computational cost clearly becomes prohibitively expensive for large N, as in the case of several thousand nodes for an ocean basin. The kriging interpolation thus needs to be performed on subdomains of N_0 nodes, where $N_0 \ll N$. This effectively replaces N by N_0 in the computational cost estimate. For the particular advection experiments performed in Section 5, we found that subdomains of 90 to 100 nodes give a comparably high accuracy with $K(h) = h^7$. For $K(h) = -h^5$ and $K(h) = h^3$, subdomains of fewer nodes may be used without a significant further degradation in accuracy. However, even with subdomain decomposition, kriging is still more costly than bicubic spline interpolation. Bermejo (1990) found that the computation of the upstream value of a scalar field using bicubic spline interpolation requires 49 long operations, if it is implemented efficiently. For kriging with a typical domain of several thousand nodes on a rectangular uniform mesh, decomposition into subdomains of 100 nodes each would lead to a total computational cost which is about 40 times that of bicubic spline interpolation. This estimate does not take into account the overlapping regions of the subdomains, as this depends on the nature of the domain partitioning.

As an illustration of how kriging works over connected subdomains, we partition our global 33×33 rectangular mesh into four identical subdomains having an intersection of width $4\Delta x$ and $6\Delta x$, resulting in subdomains of 19×19 and 20×20 grids respectively. For both these cases, ϕ_{max} remains at 100 and the fractional change in mass is less than 0.1%, after up to 10 rotations of the cosine hill. Fig. 10 compares the behaviour of ϕ_{min} obtained with the kriging system using a global domain, with those obtained using the two subdomain decompositions as well as with bicubic spline interpolation. The results show that although the dispersion is increased slightly with the two subdomains, it still remains less than that obtained with bicubic spline interpolation. The results on a 19×19 subdomain are worse than those on a 20×20 subdomain, due to the smaller intersection area.

A further saving in the computational cost comes from the accuracy of the kriging interpola-

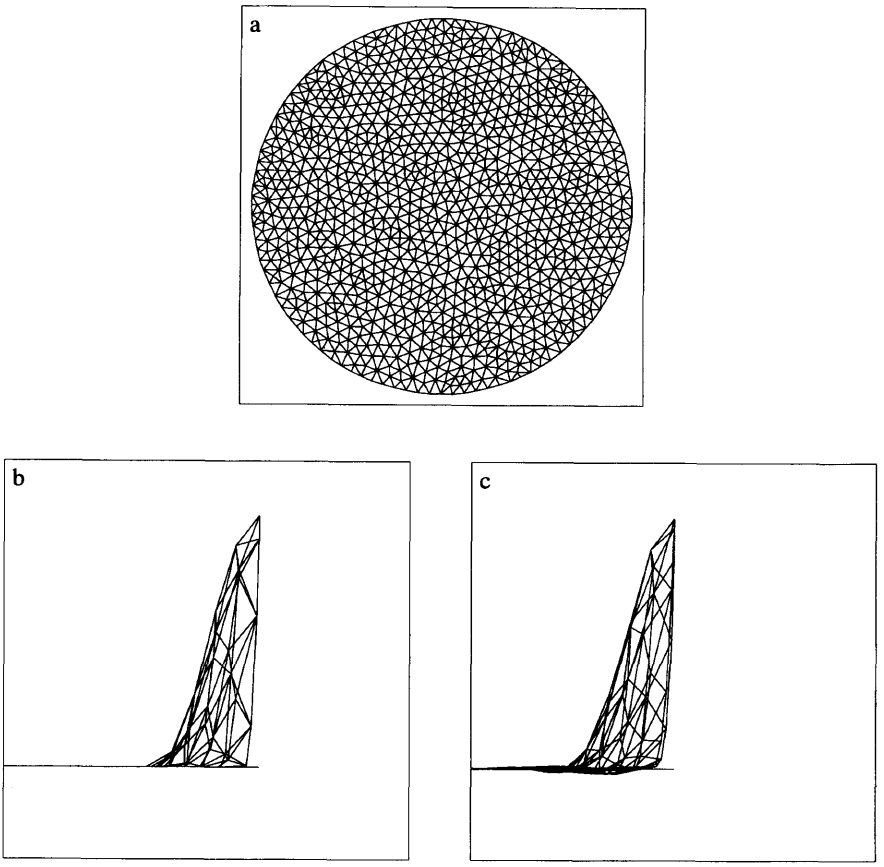

Fig. 9. (a) Mesh 4, a triangulated circle. (b) Shape of the half cosine hill with its maximum height located at the boundary at time $t = 0$, $R = 4\Delta x$, $\phi_{max} = 100$, $\phi_{min} = 0$. (c) After 10 000 time steps using a kriging interpolation scheme ($K(h) = h^7$, cubic drift), $R = 4\Delta x$, $C = 1$, $\phi_{max} = 100$, $\phi_{min} = -2$.

tion itself, as a smaller mesh is then required with kriging compared to bicubic spline interpolation. We consider a sequence of increasing rectangular mesh sizes ranging from 41×41 to 97×97, and a corresponding increase in the number of grid points under the cosine hill ranging from 81 to 441. Thus the radius of the cosine hill R is held fixed and the resolution is increased. Fig. 11 shows ϕ_{max} for the cosine hill with bicubic spline interpolation after 160 rotations. These results are compared to those obtained with kriging on a much smaller 25×25 mesh, with only 29 grid points under the cosine hill. We see that the kriging results are comparable in accuracy to that obtained with bicubic spline interpolation on a much larger mesh and a finer resolution of the cosine hill. Thus depending on the nature of the problem, a coarser mesh can be used with kriging to obtain the same level of accuracy as with bicubic spline interpolation. However, kriging is still more costly than bicubic spline interpolation: for kriging with 4 subdomains of 196 nodes each on the 25×25 mesh, bicubic spline interpolation on a 81×81 mesh achieves comparable accuracy but at approximately 10 times less cost.

Another factor that should be considered in the discussion of computational cost is mesh refinement. When local refinement is needed, such as near the boundaries of an ocean model, a triangular unstructured mesh can be constructed with significantly fewer nodes compared to a rectangular mesh, especially on the sphere. Since bicubic

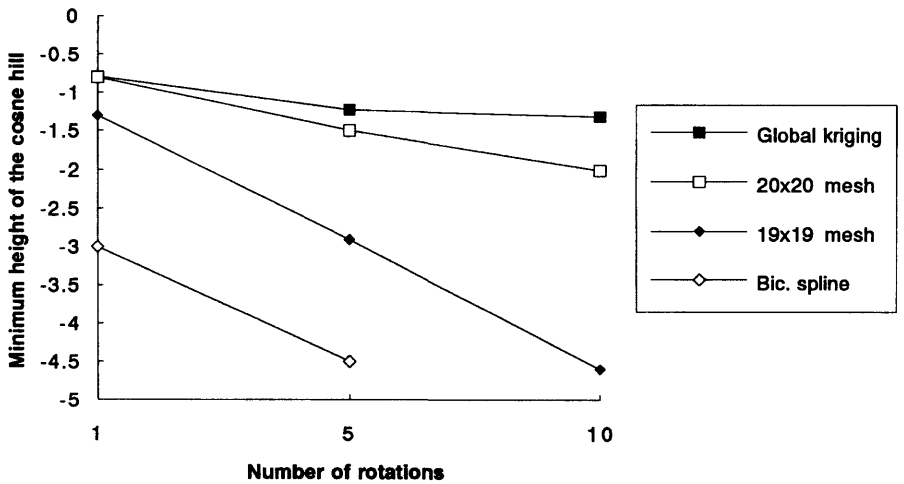

Fig. 10. Minimum values of the cosine hill for the global domain and subdomains using bicubic spline and kriging interpolation ($K(h) = h^7$, cubic drift) schemes after up to 10 rotations, $R = 4\Delta x$, $C = 1$.

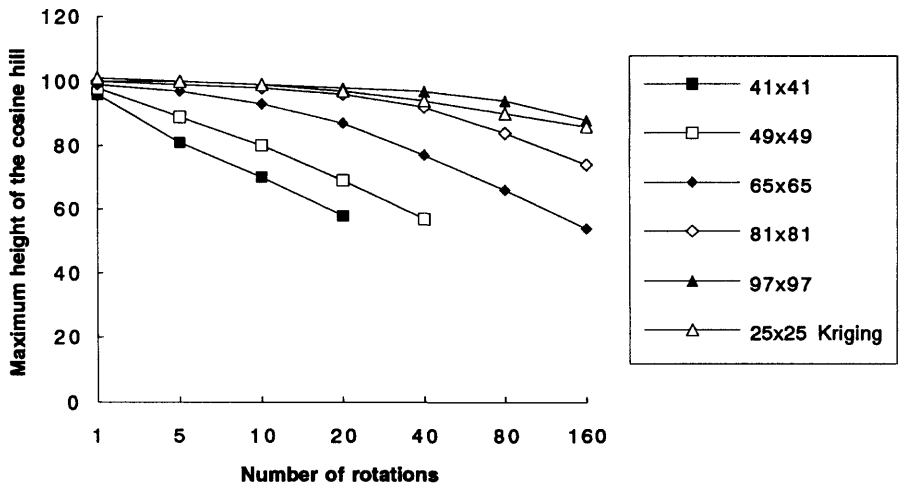

Fig. 11. Maximum values of the cosine hill after up to 160 rotations (22 752 time steps) for different meshes using bicubic spline (41 × 41 to 97 × 97 meshes) and kriging interpolation ($K(h) = h^7$, cubic drift) schemes, R constant, $C = 1$.

spline interpolation is restricted to regular meshes, this leads to a saving in computational cost for the kriging interpolation. As an example, the two meshes shown in Figs. 12a, b are used for the same advection experiments performed in Section 5. Each mesh has been optimised to give the same results for ϕ_{max} and ϕ_{min} up to 80 rotations. Bicubic spline interpolation is used on the regular mesh 5 with 5776 nodes, and kriging on the triangular unstructured mesh 6 with 426 nodes. Note that the resolution of the regular mesh becomes up to 4 times that of the unstructured mesh. When 4 subdomains are used on the triangular mesh with kriging, the bicubic spline interpolation now only becomes 5 times less expensive; in other words, kriging is still more costly. However, Staniforth and Côté (1991) noted that increasing the resolution has important implications for the relative order of the temporal and spatial truncation errors for coupled equa-

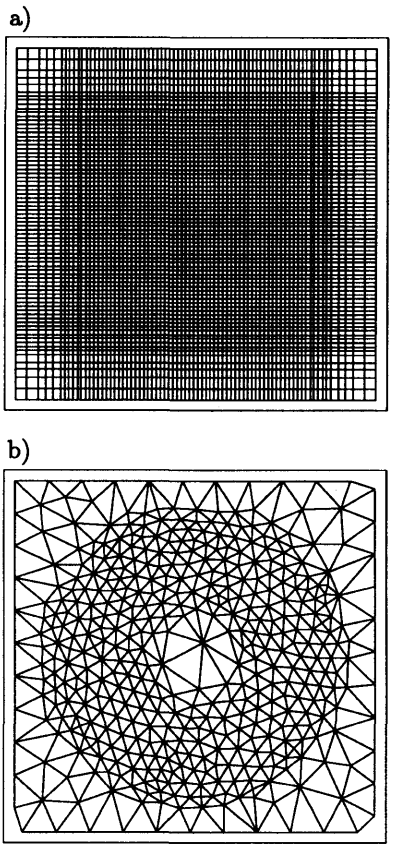

Fig. 12. (a) Mesh 5, a 76 × 76 mesh, refined in the area where the cosine hill is displaced. (b) Mesh 6, a triangular mesh refined along the cosine hill trajectory.

tions, such as the shallow water equations. In the case of semi-Lagrangian advection combined with a semi-implicit time scheme, it is possible to choose the time step such that the temporal and spatial errors are of the same magnitude. When bicubic spline interpolation is used in the semi-Lagrangian discretization of advection, the $O(\Delta t^2)$ temporal truncation errors are approximately equal in magnitude to the $O(\Delta x^4)$ spatial errors. Thus, doubling the resolution implies reducing Δt by a factor of 4 if the balance between temporal and spatial truncation errors is to be kept. Since the resolution of the regular mesh 5 is up to 4 times that of the triangular mesh 6, this implies reducing Δt by a factor of 16 on the regular grid. In this case, kriging becomes less expensive than bicubic spline interpolation. However, Staniforth and Côté (1991) assumed that the dominant source of spatial truncation error is more likely $O(\Delta x^2)$. In this case, the second doubling of resolution implies reducing Δt by a factor of 4, instead of 16. Now kriging is only marginally more expensive compared to bicubic spline interpolation. One might argue that the triangular mesh 6 is not a representative case. However, in a realistic ocean basin the area of interest often involves intense boundary currents, and mesh refinement needs to be carried out near the boundary. In this case, the regular mesh 5 is much more difficult to refine optimally since the refined area will cover practically the entire domain. In addition, the refined area on mesh 6 represents a large part of the domain. For a typical ocean mesh, the refined region is usually proportionally much smaller. The gain in node efficiency compared to a regular mesh may thus be considerably enhanced.

The computational gain with kriging might be further enhanced through the use of an adaptive mesh with an a priori error estimator (Bespalov et al., 1992). However, the use of an adapted mesh generally requires the computation of the Hessian matrix for velocity to obtain the error estimation. This in turn requires knowledge of the second derivatives for the adaptivity criteria. Due to its accuracy, kriging provides an efficient way to perform interpolation of derivatives. Fig. 13 shows the cosine hill with $R = 4\Delta x$ and its first three derivatives $(\phi, \phi_x, \phi_{xx}, \phi_{xxx})$ after 80 rotations on the unstructured triangular mesh 3 shown earlier in Fig. 8a; $K(h) = h^7$ and a cubic drift are used. The cosine hill and its derivatives have only been marginally distorted after the 11 376 time steps of the integration, thus demonstrating once again the accuracy and efficiency of kriging.

Finally, kriging may be performed efficiently on vector and parallel supercomputers. Most of the kriging codes that we developed run at about 2 GFlops on one processor of the NEC SX3-44 supercomputer at the Atmospheric Environment Service of Environment Canada. With a partitioned domain, the computation may be carried out independently on each subdomain, leading to a significant gain in computational efficiency.

8. Conclusion

By using a dual kriging interpolation scheme, we have developed a semi-Lagrangian advection

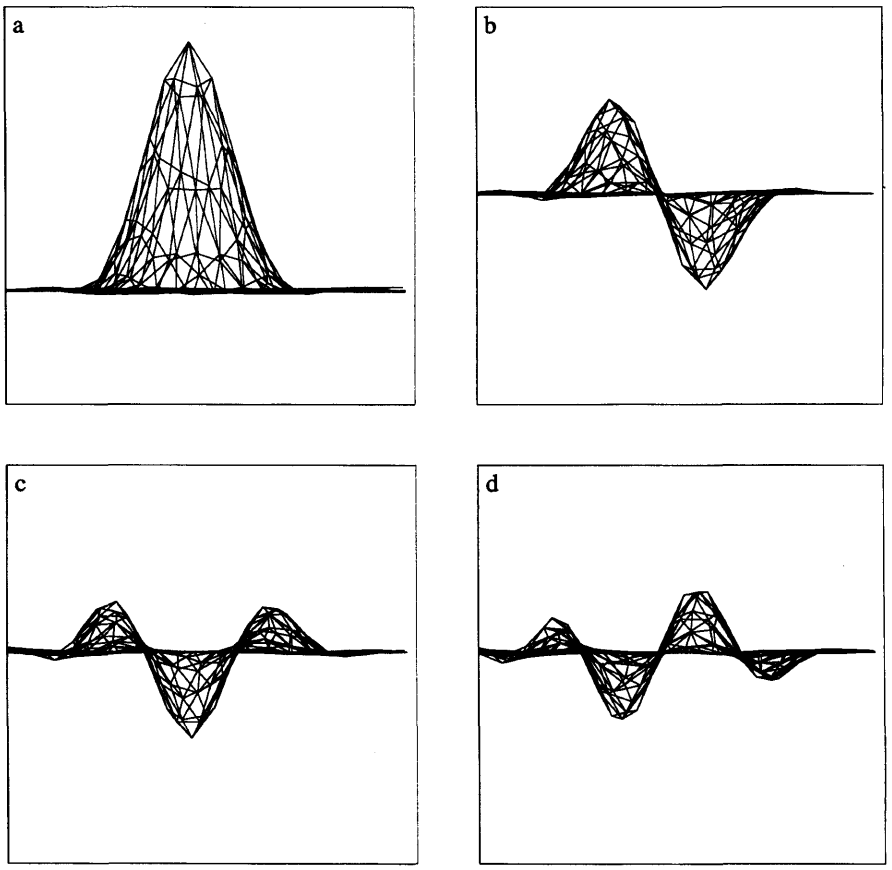

Fig. 13. (a) Shape of the cosine hill (ϕ) on mesh 3 of Fig. 8a after 80 rotations (11 376 time steps) using a kriging interpolation scheme ($K(h) = h^7$, cubic drift), $R = 4\Delta x$, $C = 1$; $(\phi_{max}, \phi_{min}) = (100, 0)$ indicated in brackets at later times. (b) First derivative ϕ_x; (39, −39). (c) Second derivative ϕ_{xx}; (21, −35). (d) Third derivative ϕ_{xxx}; (25, −27).

method which is more accurate that the $O(\Delta x^4)$ of bicubic interpolation. This level of accuracy for semi-Lagrangian advection, has not been realized before on unstructured meshes. The accuracy is especially important for ocean models compared to atmospheric models, as the time scales of interest are much longer for the ocean. The small amount of dissipation and dispersion ensures mass conservation for long simulations, without recourse to mass correction. Furthermore, the small dispersion is a significant improvement compared to general Eulerian models. This implies that unphysical artificial viscosity might be more easily avoided in coupled dynamical equations, such as the shallow water equations. The computational cost is significant, but it can be reduced through domain partitioning without a significant loss of accuracy. The use of a locally refined triangular mesh shows that the cost of kriging is reasonable compared to that obtained with bicubic spline interpolation on a regular grid. The fact that kriging applies equally well to structured as well as unstructured meshes with irregular geometry, demonstrates its excellent flexibility. Finally, the high accuracy obtained with kriging for the derivatives of a scalar field is promising for the use of adaptive meshes on irregular geometries.

9. Acknowledgement

This work is supported by grants to CAL from the Natural Sciences and Engineering Research

Council (NSERC), the Atmospheric Environment Service (AES) of Canada and FCAR (Fonds pour la Formation de Chercheurs et l'Aide à la Recherche). We gratefully acknowledge Dr. Marie-Gabrielle Vallet for help in using her grid generation package developed at CERCA (Centre de recherche en calcul appliqué) and Drs. M. Soulié and F. Trochu of Ecole Polytechnique (Montréal) for helpful discussions. The use of the computing facilities of CERCA is also acknowledged. Computing time on the NEC SX3-44 at the AES was provided by Dr. Michel Béland.

REFERENCES

Bates, J. R. and McDonald, A. 1982. Multiply-upstream, semi-Lagrangian advective schemes: Analysis and application to a multilevel primitive equation model. *Mon. Wea. Rev.* **112**, 1831–1842.

Baumgardner, J. R. and Frederickson, P. O. 1985. Icosahedral discretization of the two-sphere. *Siam J. Numer. Anal.* **22**, 1107–1115.

Bermejo, R. 1990. On the equivalence of semi-Lagrangian and particle-in-cell finite element methods. *Mon. Wea. Rev.* **118**, 979–987.

Bespalov, A., Kuznetsov, Y., Pironneau, O. and Vallet, M. G. 1992. Fictitious domains with separable preconditioners versus unstructured adapted meshes. *Impact of Computing in Science and Engineering* **4**, 217–249.

Christakos, G. 1984. On the problem of permissible covariance and variogram models. *Water Resources Research* **20**, 251–265.

Cullen, M. J. P. 1974. Integration of the primitive equations on a sphere using the finite element method. *Quart. J. Roy. Soc.* **100**, 555–562.

Daley, R. 1991. *Atmospheric data analysis.* Cambridge University Press.

Delfiner, P. and Delhomme, J. P. 1973. Optimum interpolation by kriging. *Proceedings of NATO ASI, Display and analysis of spatial data* eds. J. C. Davis and M. J. McCullagh, pp. 96–114, John Wiley, New York.

Delfiner, P. 1979. The intrinsic model of order *k*. *Notes de cours C-77.* Centre de Géostatistique, Ecole des Mines de Paris, Fontainebleau, France.

Dubrule, O. 1981. *Krigeage et spline en cartographie automatique. Application à des exemples pétroliers.* Thèse de Docteur Ingénieur. Centre de Géostatistique, Ecole des Mines de Paris, Fontainebleau, France.

Gilbert, R., Carrier, R., Benoit, C., Soulié, M. and Schiettekatte, J. 1990. *Applications of dual kriging in human factors engineering. Advances in industrial ergonomics and safety (II).* Biman Das, ed. Taylor & Francis, London.

Heikes, R. and Randall, D. A. 1995a. Numerical integration of the shallow-water equations on a twisted icosahedral grid. Part I: basic design and results of tests. *Mon. Wea. Rev.* **123**, 1862–1880.

Heikes, R. and Randall, D. A. 1995b. Numerical integration of the shallow-water equations on a twisted icosahedral grid. Part II: a detailed description of the grid and an analysis of numerical accuracy. *Mon. Wea. Rev.* **123**, 1881–1887.

Journel, A. G. and Huijbregts, C. J. 1978. *Mining geostatistics.* Academic Press.

Karpic, S. R. 1994. A spline-based semi-Lagrangian method for advection-dominated transport equations on triangular meshes. *Proceedings, 2nd Annual Conf. of the CFD Society of Canada,* Toronto. J. J. Gottlieb and C. R. Ethier (eds.), 91–98.

Krige, D. G. 1951. A statistical approach to some basic mine valuation problems on the Witwatersrand. *J. Chem. Metall. Min. Soc. S. Afr.* **52**, 119–139.

Leslie, L. M. and Purser, R. J. 1991. High-order numerics in a three-dimensional time-split semi-Lagrangian forecast model. *Mon. Wea. Rev.* **119**, 1612–1623.

Lorenc, A. C. 1986. Analysis methods for numerical weather prediction. *Quart. J. Roy. Soc.* **112**, 1177–1194.

Matheron, G. 1973. The intrinsic random functions and their applications. *Adv. Appl. Prob.* **5**, 439–468.

Matheron, G. 1980. *Splines et krigeage: leur équivalence formelle.* Rapport N-667, Centre de Géostatistique, Ecole des Mines de Paris, Fontainebleau, France.

Mcdonald, A. 1984. Accuracy of multiply-upstream semi-Lagrangian advective schemes. *Mon. Wea. Rev.* **112**, 1267–1275.

McDonald, A. 1987. Accuracy of multiply-upstream semi-Lagrangian advective schemes (II). *Mon. Wea. Rev.* **115**, 1446–1450.

McDonald, A. and Bates, J. R. 1987. Improving the estimate of the departure point position in a two-time level semi-Lagrangian and semi-implicit scheme. *Mon. Wea. Rev.* **115**, 737–739.

Morton, K. W. 1985. Generalized Galerkin methods for hyperbolic problems. *Comp. Meth. Appl. Mech. Eng.* **52**, 847–871.

Pudykiewicz, J. and Staniforth, A. 1984. Some properties and comparative performance of the semi-Lagrangian method of Robert in the solution of the advection-diffusion equation. *Atmos. Ocean.* **22**, 283–308.

Pudykiewicz, J., Benoit, R. and Staniforth, A. 1985. Preliminary results from a partial LRTAP model based on an existing meteorological forecast model. *Atmos. Ocean.* **23**, 267–303.

Purnell, D. K. 1976. Solution of the advective equation by upstream interpolation with a cubic spline. *Mon. Wea. Rev.* **104**, 42–48.

Purser, R. J. and Leslie, L. M. 1988. A semi-implicit semi-Lagrangian finite-difference scheme using high order spatial differencing on a nonstaggered grid. *Mon. Wea. Rev.* **116**, 2069–2080.

Raviart, P. A. 1985. An analysis of particle methods. *Numerical methods of fluid dynamics*, vol **1127**, F. Brezzi, ed. Springer-Verlag, 324 pp.

Robert, A. 1981. A stable numerical integration scheme for the primitive meteorological equations. *Atmos. Ocean.* **19**, 35–46.

Robert, A. 1982. A semi-Lagrangian and semi-implicit numerical integration scheme for the primitive meteorological equations. *Jpn. Meteor. Soc.* **60**, 319–325.

Robert, A., Henderson, J. and Turnbull, C. 1972. An implicit time integration scheme for baroclinic models of the atmosphere. *Mon. Wea. Rev.* **100**, 329–335.

Sadourny, R., Arakawa, A. and Mintz. 1968. Integration of the non-divergent barotropic vorticity equations with an icosahedral-hexagonal grid for the sphere. *Mon. Wea. Rev.* **96**, 351–356.

Sadourny, R. 1972. Conservative finite-difference approximations of the primitive equations on quasi-uniform spherical grids. *Mon. Wea. Rev.* **100**, 136–144.

Staniforth, A. and Pudykiewicz, J. 1985. Reply to comments on and addenda to some properties and comparative performance of the semi-Lagrangian method of Robert in the solution of the advection-diffusion equation. *Atmos. Ocean.* **23**, 195–200.

Staniforth, A. and Temperton, C. 1986. Semi-implicit semi-Lagrangian integration schemes for a barotropic finite-element regional model. *Mon. Wea. Rev.* **114**, 2078–2090.

Staniforth, A. and Côté, J. 1991. Semi-Lagrangian integration schemes for atmospheric models: a review. *Mon. Wea. Rev.* **119**, 2206–2223.

Temperton, C. and Staniforth A. 1987. An efficient two-time level semi-Lagrangian semi-implicit integration scheme. *Quart. J. Roy. Meteor. Soc.* **113**, 1025–1039.

Trochu, F. 1993. A contouring program based on dual kriging interpolation. *Engineering with Computers* **9**, 160–177.

Williamson, D. L. 1968. Integration of the barotropic vorticity equation on a spherical geodesic grid. *Tellus.* **20**, 642–653.

Williamson, D. L. 1970. Integration of the primitive barotropic model over a spherical geodesic grid. *Mon. Wea. Rev.* **98**, 512–520.